AIAA AVIATION Forum
June 15-19, 2020, VIRTUAL EVENT
AIAA AVIATION 2020 FORUM

10.2514/6.2020-2988

Effect of Vortex Shedding on the Aerosolization of a Particle from a Hill using Large Eddy Simulation

Amit Sharma[1] and Urmila Ghia[2]
The University of Cincinnati, Cincinnati, Ohio, 45221, USA

Leonid Turkevich[3]
National Institute of Occupational Safety and Health, Centers for Disease Control and Prevention, Cincinnati, Ohio, 45200, USA

Motivated by recent experiments on the dustiness of nanoscale powders, this research reports on a numerical study of powder aerosolization inside the Venturi Dustiness Tester (VDT). In particular, we study the effect of vortex shedding on the aerosolization of a test particle from a powder hill at Reynolds number of 20,000 in the powder holding device attached to VDT. The powder holding tube is represented as a cylindrical tube with a hemispherical (powder) hill situated within. A test particle is positioned at various locations on the hill. We study the flow behavior past the hemispherical obstruction in the tube and its influence on the aerodynamic forces experienced by a test particle located at various positions on the obstruction. The frequency of the vortex shedding from the bump yields a Strouhal number St = 0.2. The peak frequency associated with the particle positioned at the top of the bump is comparable to that associated with the bump alone. We calculate the time-dependent drag, lift, and moment on the test particle, each of which is strongly influenced by the vortex shedding from the hill. The mean values of drag, lift, and moment on the test particle characterize its aerosolization.

I. Nomenclature

u	=	average velocity in nozzle	d	=	diameter of particle
St	=	Strouhal number	k	=	slope of power spectral density
f	=	frequency	C_f	=	Mean skin friction coefficient
D	=	diameter of pipe	$C_{f.}$	=	Mean pressure coefficient

II. Introduction

There is growing concern about the potential health impact of inhaled nanomaterials [7, 21, 25]. Controlled laboratory measurements may indicate the severity of the airborne release of nanoparticles.

Dustiness is the propensity of a finely divided solid (a powder) to become airborne (dust) as a result of the mechanical or aerodynamic stimulus [19, 25]. Standardized dustiness testing techniques involve the application of a specified type and amount of mechanical energy to a specified amount of test material for a specified time (in order to overcome the adhesive binding forces within the test powder) and thus disperse pre-existing particles from the test powder into the air; the amount of dust released is then quantified. A variety of methods have historically been utilized to measure dustiness [14, 15,].

[1] Graduate Student, Mechanical and Materials Engineering, sharm2a2@mail.uc.edu.
[2] Professor Emerita, Mechanical and Materials Engineering, ghiau@ucmail.uc.edu.
[3] Senior Service Fellow, EPHB/DFSE/NIOSH/CDC, llt0@cdc.gov.

These techniques, *e.g.*, falling powder [1, 3, 8, 10, 16, 17, 24, 26] and rotating drum [5, 6, 9, 18] require the use of relatively large quantities of powder, typically, 10_2 - 10_3 grams per test. Such quantities preclude the testing of nanoscale powders. These methods impart gentle mechanical agitation to the powder, and the aerodynamics tend to involve large-scale eddies. In both methods, aerosolization is gravity-driven, and the maximum velocities of the particles achieved are ~ 1 m/s.

Venturi dustiness test (VDT) method:
A qualitatively different method using the Venturi Dustiness Tester (VDT) was introduced by Boundy *et al*. [4] in order to test pharmaceutical powders. The aim was to utilize small quantities (~ 5 mg) of powder under confined conditions (so as not to expose the test operator to pharmacologically active material). Evans *et al.* [13] used the VDT (Fig. 1) to measure the dustiness of a series of fine and nanoscale powders (e.g., carbon nanotubes, nanofibers, carbon blacks, metal oxides, metallic nanoparticles).

Powder is placed in a holding tube, exterior to, but piercing the dispersion chamber. Air is introduced into the dispersion chamber via the holding tube, resulting in nozzle airflow with velocity u ~ 70 m/s. Aerosolization presumably occurs via aerodynamic lift and pneumatic drag mechanisms acting on the powder; aerosolization proceeds under turbulent conditions (Reynolds number Re ~ 10_4), whereas in the gentle tests, the airflows are larger scale and are in the laminar regime. A more detailed picture of the powder holding tube is shown in the schematic in Figure 2.

When air enters the dispersion chamber, the primary flow is along the horizontal tube of the 'tee', although a small flow is also drawn down the vertical tube of the 'tee'. This combined airflow aerosolizes the powder and sweeps it into the chamber. The present research numerically investigates the aerosolization in the powder holding tube, where the geometry has been simplified by neglecting the vertical 'tee' tube (shown in Figure 2). Specifically, we study the effect of vortex shedding on the aerosolization of a test particle from a hill at Reynolds number of 20,000. Figure 3 shows the powder holding tube, represented as a cylindrical tube with a hemispherical (powder) hill situated within.

In order to evaluate how aerosolization is likely to occur, we investigate the aerodynamic forces experienced by a test particle at various locations on the surface of the powder hill (Figure 4). We calculate the time-dependent drag, lift, and moment on the test particle, presumably dominated by the vortex shedding from the hill. This will help in quantifying the aerosolization of the particle.

Fig. 1. The Venturi Dustiness Test (VDT) Apparatus (entrance tube at right) [16].

Previous Work:
Dubey *et al.* [11] conducted a numerical study of the aerosol dispersion and sampling in the Venturi apparatus. This accurately reproduced the aerodynamics of the VDT (both dispersion and sampling phases). However, it presupposed the aerosolization of the powder which takes place within the VDT tube.

Palakurthi [22] and Palakurthi *et al.* [23] studied the aerodynamics of flow over a powder hill, but only in the laminar regime (Re < 1000). They found significant alteration of the drag and enhancement of the lift on a test particle situated at various locations on the hill.

Our study extends this earlier laminar study to more relevant flows (Re ~ 20,000), where vortex shedding from the powder obstruction is expected to occur; vortex shedding presumably dominates the breakdown of the powder hill and the aerosolization of the powder.

Wood *et al.* [32] have studied (using both wind tunnel experiments and Large-Eddy Simulations (LES)) turbulent flow (Re ~ 50,000) past a hemisphere on a planar substrate. They observed two distinct vortex shedding processes: a) separation of the boundary layer at the top of the hemisphere, leading to a detachment of 'arch-like' vortices; b) von Karman vortex shedding from the sides of the hemisphere, this latter shedding is intermittently symmetric (simultaneous shedding from both sides of the hemisphere), or alternating (from either side of the hemisphere).

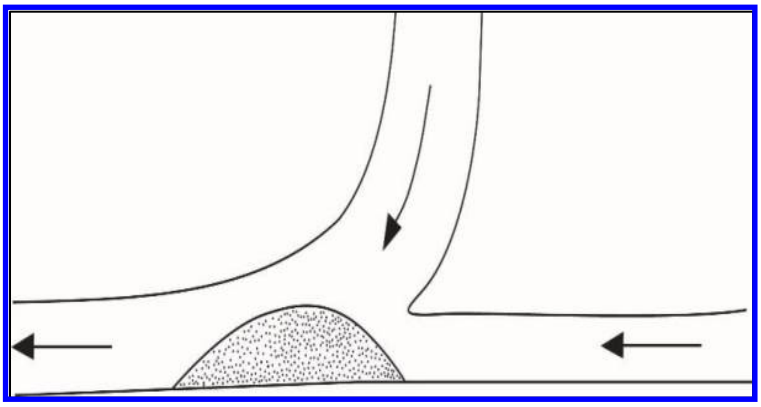

Fig. 2. Schematic of VDT entrance tube—powder is initially placed at the base of the 'tee'; turbulent air flows from the right (and small quantities from the top) to the left, aerosolizing the powder [16].

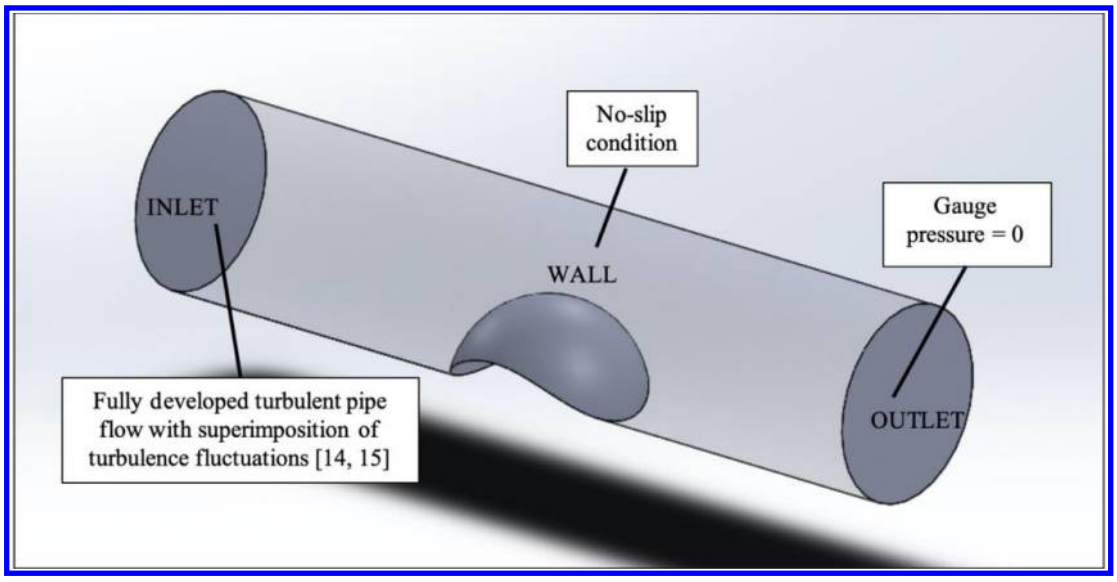

Fig. 3. Geometry and boundary conditions for holding tube with hemispherical (powder) hill.

III.Method

Large-Eddy Simulation (appropriate for Re ~ 20,000) is performed using ANSYS Fluent 19.2. The flow is assumed to be incompressible. The simulation domain is a circular pipe (D = 4 mm) with a wall-mounted hemispherical obstruction (R = 2 mm). The inlet boundary conditions (Fig. 3) consist of the fully developed turbulent pipe flow solution (obtained from a RANS simulation interpolated to the LES grid) with synthetic turbulence fluctuations superimposed on this inlet condition [12, 20]; and zero-gauge pressure at the outlet as shown in Figure 3. Our hybrid mesh (a combination of structured grid, far from the bump, and unstructured grid near the bump) consists of ~ 8 million grid points. The time step used is 10^{-8} sec., based on the requirement that CFL number < 1. The sweep time (time for fluid to traverse the length of the pipe) is $\Delta t \sim 3 \times 10^{-3}$ sec. The LES simulations were conducted for a duration of 6 sweeps times.

IV.Results and Discussion

This research studies the drag, lift, and moment behavior of the particle (d = 0.1 mm) positioned at various locations on the bump. We first study the flow behavior with no particle on the bump. We then introduce a particle at the top of the bump. Finally, we vary the location of the particle on the bump.

Pipe with a bump: no particle vs. particle at the top of the bump

We first study the main physical flow characteristics of vortex shedding from the bump. We expect that this vortex shedding will affect the drag, lift, and the moment of the particle when it is positioned at various locations on the bump. Savory and Toy [30] have systematically mapped the various distinct flow features prevailing in unsteady turbulent flow past a hemisphere. Wood *et al.* [32] confirmed the results as Savory and Toy using experiment and large-eddy simulation. We initially verify that this description remains valid for laterally confined flow past the hemispherical obstruction (i.e. flow past an obstruction in a tube). Figures 5a, b shows the contours of unsteady streamwise velocity obtained from our large eddy simulation; shown is the symmetry plane in the axial direction that bisects the hemisphere (z-plane = 0): a) hemisphere alone, b) hemisphere with test particle at the top.

We identify 7 regions upstream and downstream of the bump (Fig. 5a), consistent with the identification of Wood et al. [32]. Upstream (1), a horse-shoe vortex forms, due to the separation of the boundary layer from the wall of the pipe (1). This is initiated at the bottom wall of the pipe and penetrates the gap between the bump and sidewalls of the pipe. This vortex formation arises from the positive pressure gradient immediately in front of the obstructing bump.

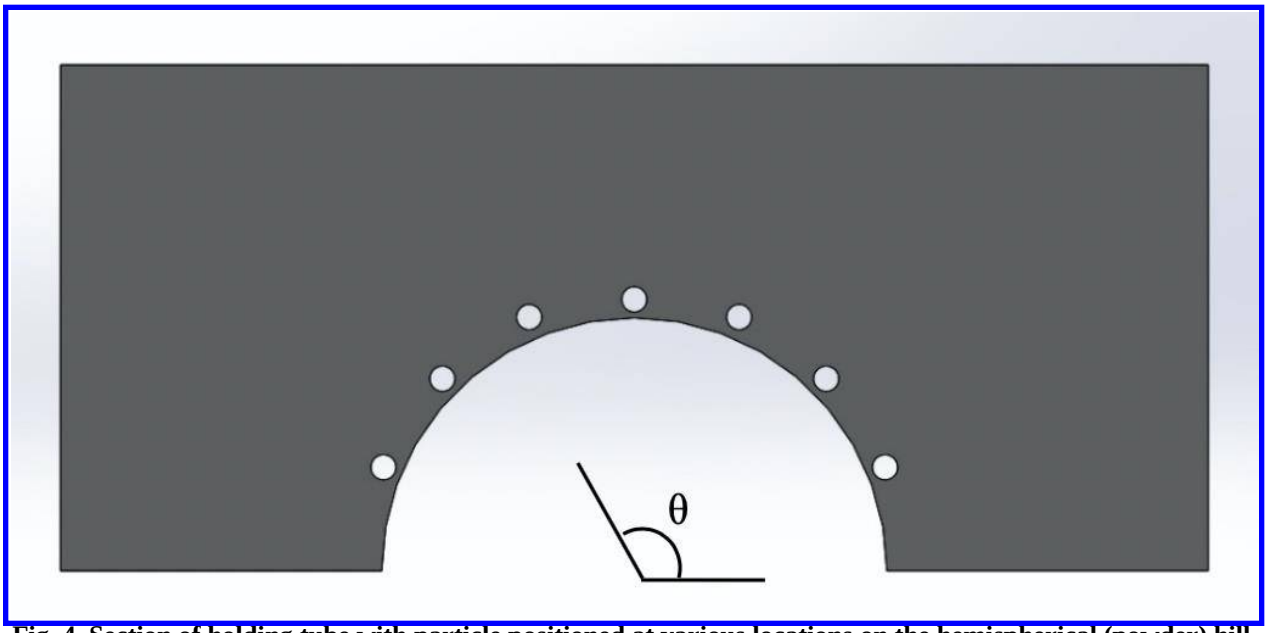

Fig. 4. Section of holding tube with particle positioned at various locations on the hemispherical (powder) hill.

The stagnation point (2) occurs at the lower front surface of the bump ($\theta \sim 160^o$). In region 3, strong vorticity is generated in the vicinity of the bump. The flow separates (4) ($\theta \sim 90^o$). Downstream (in the wake of the bump) is the recirculation zone and the outer flow field (5), which comprises of strong shear layer vorticity (6) and reattachment point (7). Kelvin-Helmholtz vortices are produced by the strong shear-layer vorticity and travel downstream. The size of the streamwise recirculation zone is quantified by the location of the reattachment point.

The vortical structure may be visualized by utilizing q-criterion iso-surfaces, for the flow past the obstruction alone (Figure 6) and with a test particle at the top of the obstruction (Figure 7). In both cases, the upstream near wall flow is dominated by a horseshoe vortex forming a necklace and spilling through the gap (between the obstruction and the side walls of the pipe) into the wake of the obstruction. The flow is detached from the obstruction (along a vertical equator), leading to vortex roll-up. These rolled-up vortices merge with the horseshoe vortex to form a large entangled vortical hairpin.

Figure 7c shows a top view of the vortex shedding from the particle, which then merges with the larger vortical structure from the obstruction.

Introduction of the test particle generates additional alternating vortex shedding (Figure 8b). Hence, the flow past the hemispherical obstruction with test particle exhibits (Figure 8a) two recirculation zones: downstream of the bump, and downstream of the particle.

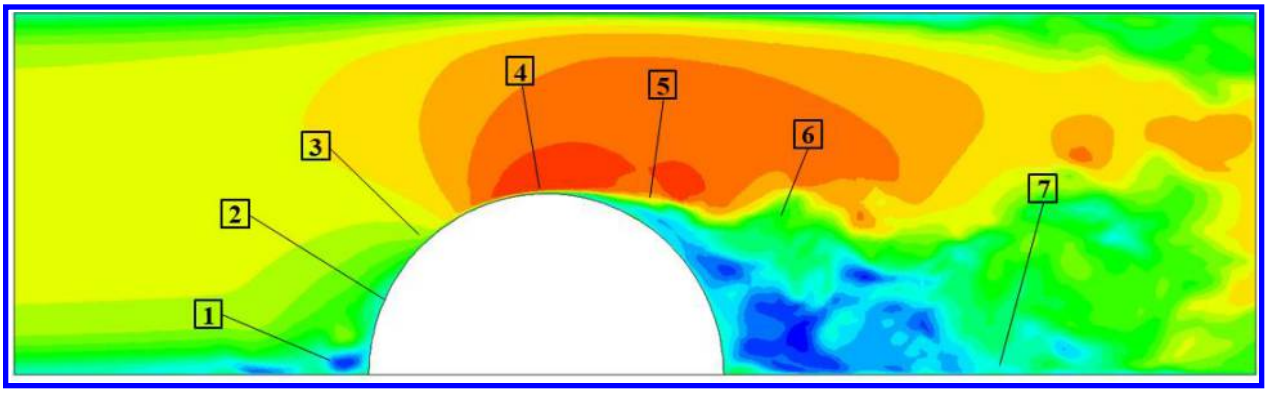

Fig. 5a. Streamwise contours of flow past a hemispherical obstruction in a tube (our LES results), with regions identified as in Wood *et al.* [32].

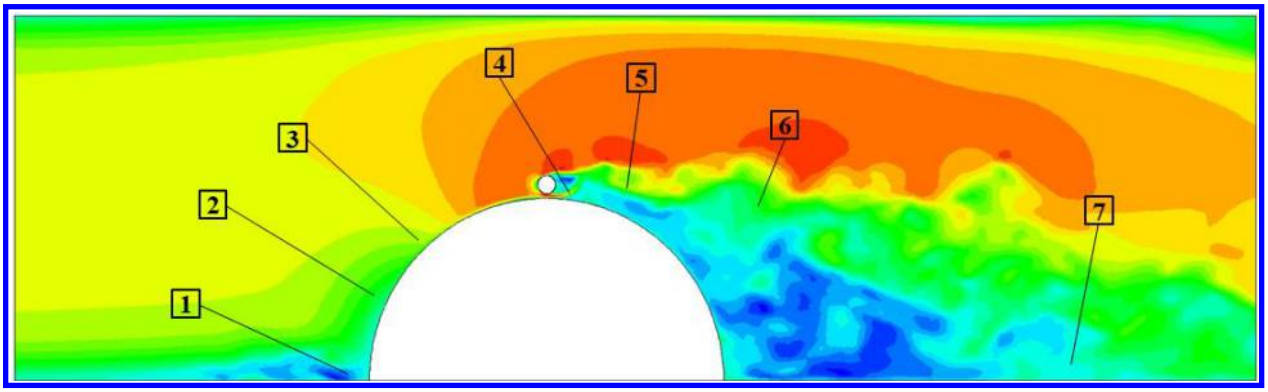

Fig. 5b. Streamwise contours of flow past a hemispherical obstruction in a tube with test particle at the top (our LES results).

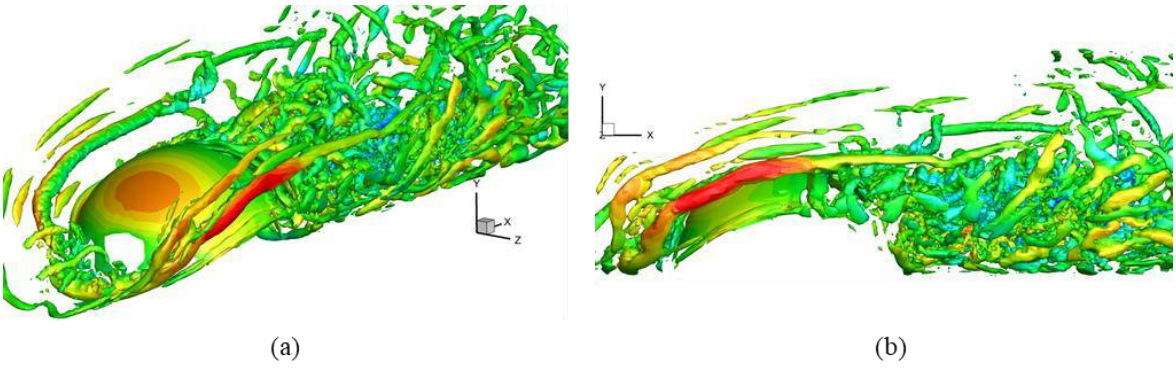

Fig. 6. Snapshot of vortical structure, visualized via q-criterion iso-surfaces (colored by vertical velocity), for hemispherical obstruction: a) isometric view, b) view along the axial direction.

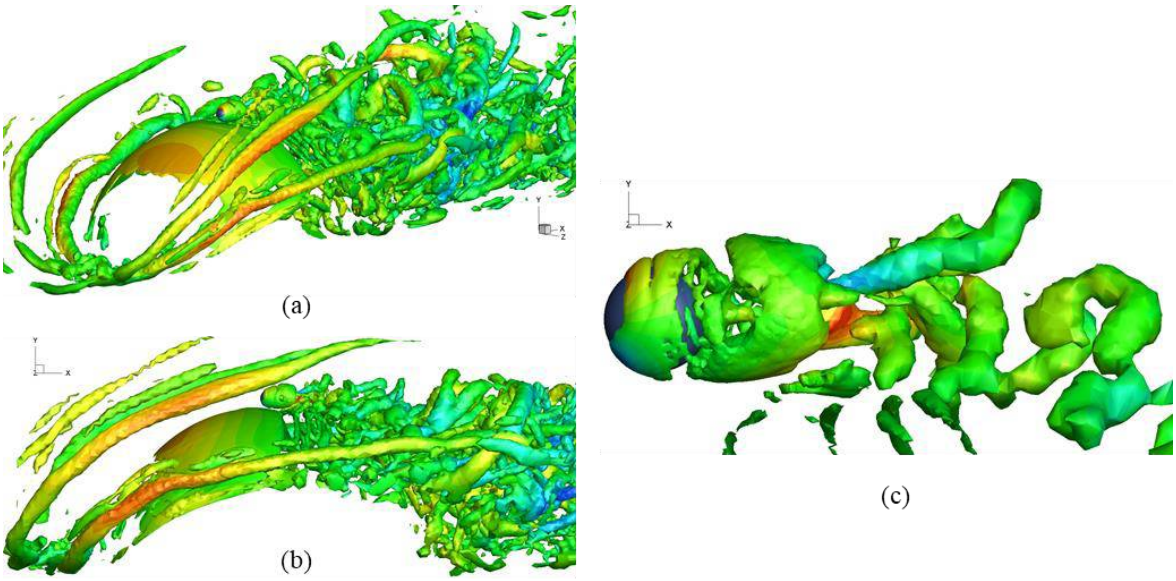

Fig. 7. Snapshot of vortical structure, visualized via q-criterion iso-surfaces (colored by vertical velocity), for hemispherical obstruction with particle at the top: a) isometric view, b) view along the axial direction.

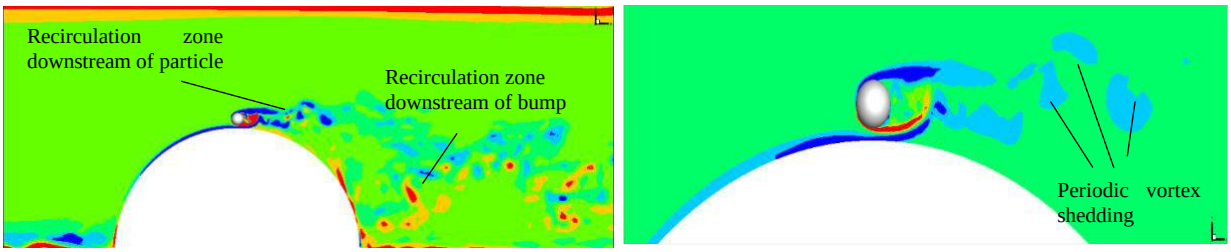

a) Recirculation zone **b) Vortex shedding behind the particle**

Fig. 8. Recirculation zones and vortex shedding behind particle on top of the obstruction.

To better identify the dynamics of the vortex shedding, we have examined the streamwise velocity spectrum (Figure 9) at a point in the center of the pipe, located in the wake of the bump (at x = 1.36 D, y = 0, z = 0). This is the location where detachment of arch-type vortices is detected, due to the separation of the boundary layer at the top of the bump. The PSD exhibits a dominant peak frequency at f ~ 7670 Hz with the corresponding Strouhal number of 0.25.

The power spectrum for the flow at this location is hardly changed with the introduction of the test particle (Figure 10). However, changes in the power spectrum are observed when the flow is sampled at a location, P1, downstream of the test particle (at x = 0.3 D, y = 1.25 D, z = 0)

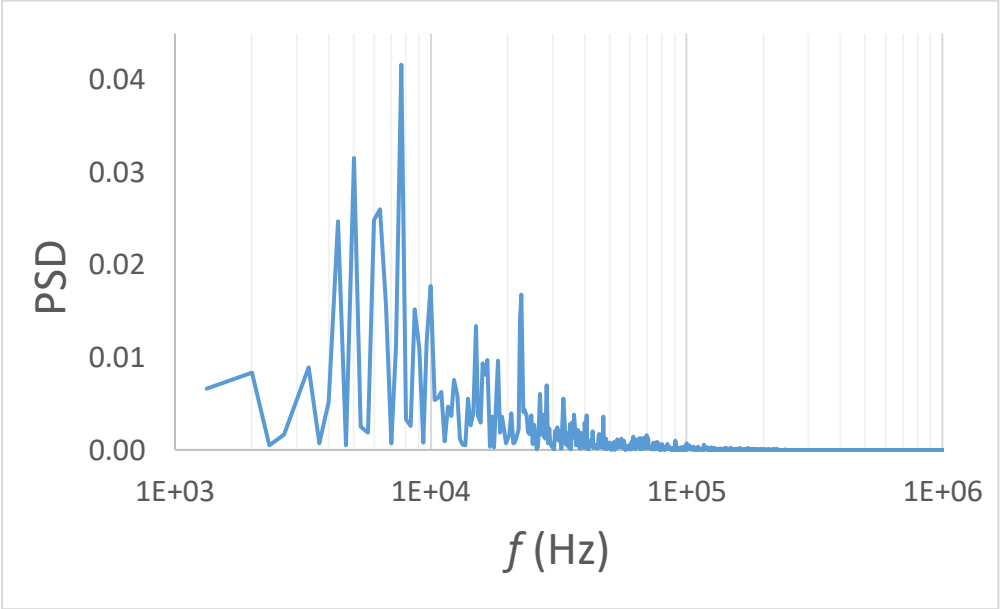

Fig. 9. Power spectral density in the wake of hemispherical obstruction.

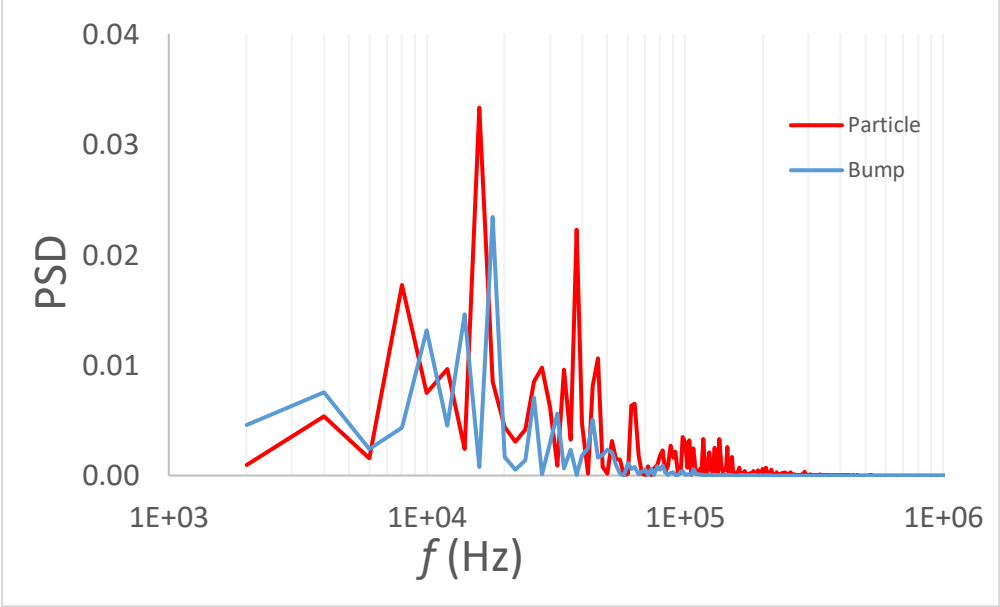

Fig. 10. Power spectral density in the wake of hemispherical obstruction and test particle.

Figure 10 shows the power spectral density for the hemisphere obstruction with particle at the top. It is evident from the figure that probe located at x/D = 0.3 near the particle exhibits dominant peak frequency of f ~ 16000 Hz. The peak frequency of f ~ 18000 Hz is also detected at the downstream probe x/D =1.36 where its magnitude is lower that the first probe peak frequency. Bakic [2] experimentally observed an absence of a well-defined frequency with the shear layer instability, but rather it exhibits subharmonics of the natural instability frequency.

A time-averaged picture does not capture all the complexities of these intricate vortex processes. We defer discussion of the streamlines and velocity contours to the next section. Figure 11 displays the time-averaged Reynolds stresses (in the symmetry midplane) for the flow past the hemisphere (with no test particle)—there are no significant changes to these stresses with the introduction of the test particle.

All stresses (diagonal <u'u'>, <v'v'>, <w'w'>, and shear <u'v'>) are enhanced in the large recirculation zone, downstream of the obstruction; this region of enhanced Reynolds stresses originates from the flow separation at the top of the obstruction. The normal stresses are confined to the wake behind the obstruction; the shear stress is maximal at a height comparable to the height of the obstruction. Upstream of the obstruction, all stresses exhibit an enhancement in the well-defined upstream recirculation zone which serves to initiate the vortex necklace. These Reynolds stress distributions are comparable with those measured experimentally by Wood *et al.* [32].

Grid Independence

We have examined the grid dependence of our results for three grids, with a refinement ratio = 1.2 (coarse: N = 4.2 x 10_6; fine: N = 7.4 x 10_6; finest: N = 12.8 x 10_6), using the axial velocity profile at two locations along the pipe: a) x/D = 0, *i.e.* at the midpoint of the bump (Fig. 12a); b) x/D = 0.067, *i.e.* in the recirculation zone downstream of the bump (Fig. 12b). The relative errors of the L2 norm are: 0.0377 (coarse to fine) and 0.0058 (fine to finest) at x/D = 0, and 0.0927 (coarse to fine) and 0.0239 (fine to finest) at x/D = 0.67.

We have also measured (Fig. 13) the LES index quality just above the centerline of the pipe (y/D = 0.0023), along the entire length of the pipe, for all three grids, and have verified that $IQ_{LES} > 0.8$, as recommended by Celik *et al.* [33].

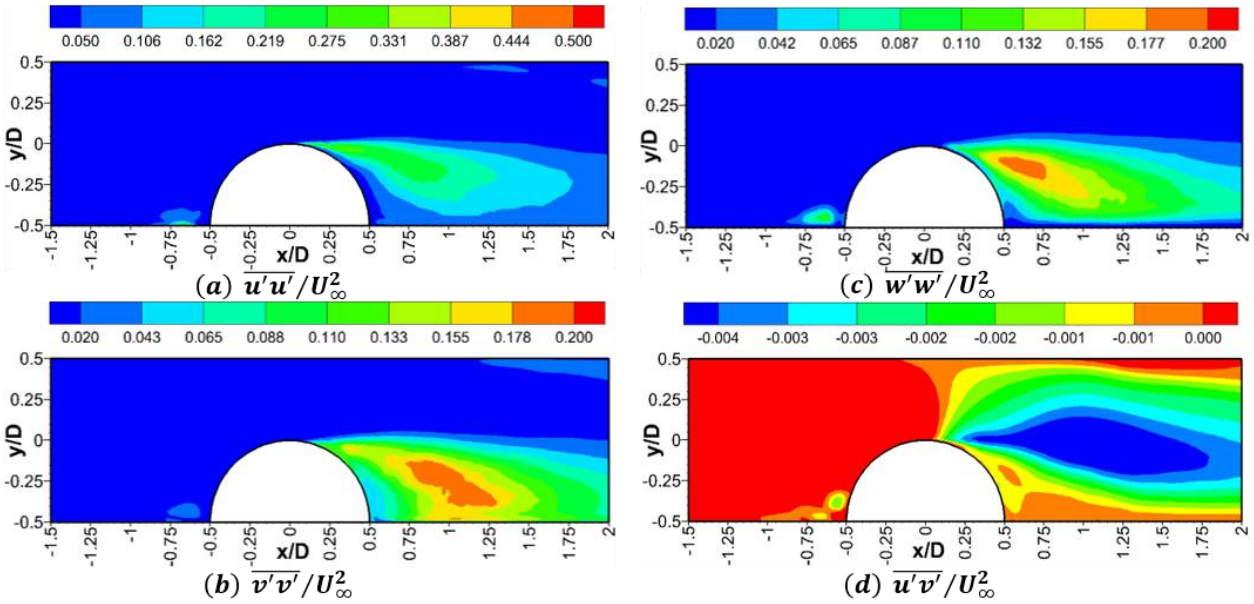

Fig. 11. Time-averaged Reynolds stresses (only hemispherical obstruction).

Aerodynamic Forces on the Test Particle

With the introduction of the test particle, the time-averaged flow exhibits subtle changes, and these subtle changes ultimately translate into a variation in the aerodynamic forces (drag, lift and moment) with location of the test particle.

Figure 14 displays the mean streamwise velocity contours (in the symmetry midplane, z = 0) in the absence of the test particle (Fig. 14a) and with the test particle introduced at various angles, α, around the hemispherical obstruction. The introduction of the test particle has minimal effect on the streamwise velocity contours. Recirculation zones are detected upstream (small: $-0.9 < x/D < -0.5$) and downstream (large: $0.5 < x/D < 1.5$) of the obstacle. Separation of the flow (near the apex of the obstruction) is characterized by a 'flag' of increased streamwise velocity.

Figure 15 displays similar mean wall-normal velocity contours. As fluid is diverted over the obstacle, the upward velocity increases ($-0.45 < x/D < -0.15$ and $-0.25 < y/D < 0$); this is unaffected by the introduction of the test particle, except (Fig. 15g) when the test particle is located directly in this vertical flow region. The test particle itself acts as an obstruction, with enhanced vertical velocity; we note that not all of the fluid is diverted over the test particle, as some of the fluid is diverted into the gap between test particle and obstacle (again, an artifact of our simulation geometry).

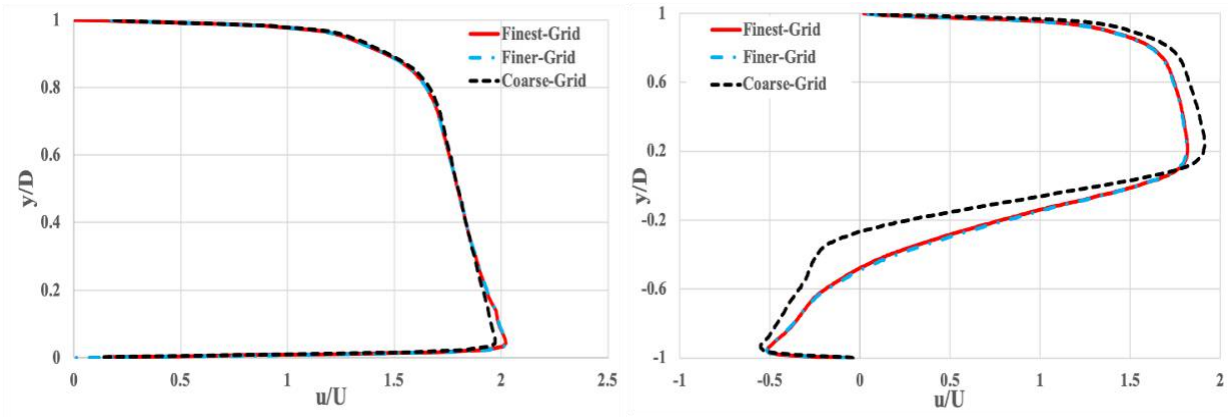

Fig. 12. Velocity profile u(y) at (a) x/D = 0 & (b) x/D = 0.67.

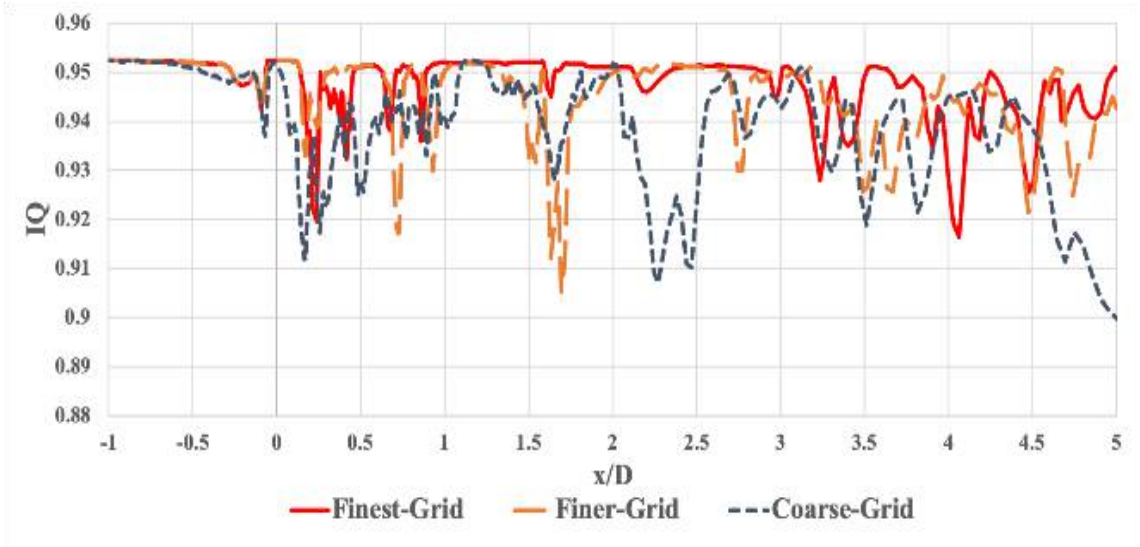

Fig. 13. $IQ_{LES}(x)$ just above the middle of the pipe (y/D = 0.0023) for the three grids.

Streamlines of these flows are shown in Figure 16. The recirculation region is more well-defined than was measured by Wood *et al.* [32]), presumably due to the confined pipe-flow geometry; it is also larger (trivial effect of different Re). The introduction of the test particle significantly extends the reattachment length (except for $\alpha \sim 112.5_o$); this is quantified in Table 1. The stagnation point (angle on the hemisphere) is unaltered and is close to $\theta = 166_o$ as measured by Wood *et al.* [32]. The flow separation point (angle on the hemisphere) is unaltered, except when the test particle is located just upstream ($\alpha \sim 112.5_o$) of the natural separation. We believe that the anomalies associated with this location of the test particle are artifacts due to the finite size of the test particle in our simulations.

Figures 17, 18, and 19 show the respective time histories of drag, lift, and moment on the test particle located ($\theta = 90_o$) at the top of the bump; we have used a moving-average smoothing with $\Delta t = 10^{-5}$ sec to remove higher frequency turbulent fluctuations. Oscillatory behavior at f ~ 6 - 7 kHz is probably due to shear-layer instability (vortex shedding) from the bump. These results quantitatively indicate the high frequency oscillatory forces on the particle arising from the shear layer instability. Similar results were also found by Tomboulides *et al.* [31] at Re = 20,000.

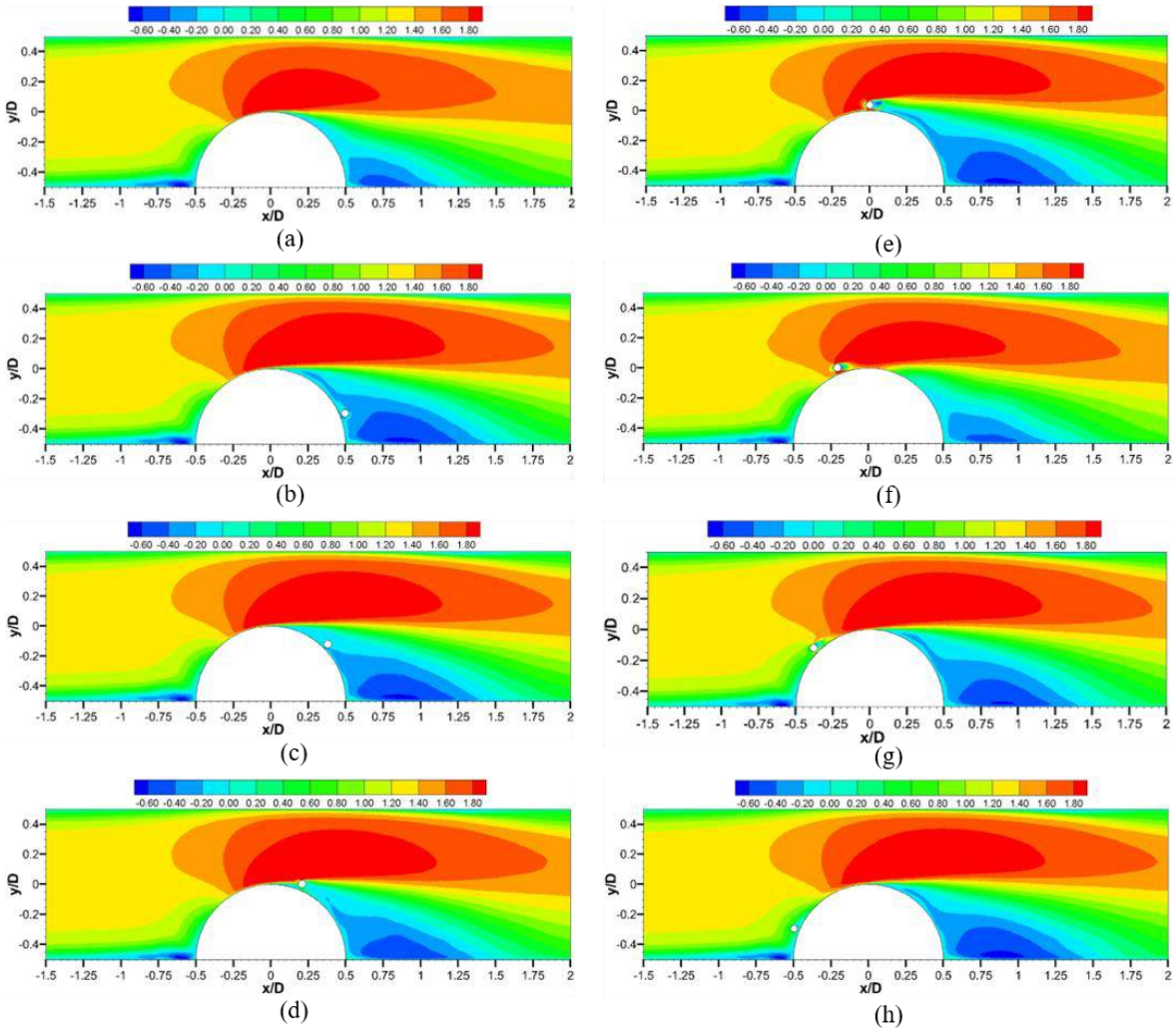

Fig. 14. Mean streamwise velocity contours.

The net drag and lift forces, and net moment are non-zero, with the mean values $F_{drag} \sim 1.66 \times 10^{-4}$ N, $F_{lift} \sim 4.04 \times 10^{-6}$ N, $\tau \sim -2.74 \times 10^{-8}$ N-m. Palakurthi *et al.* [23] had found that, for laminar flow, the values of these quantities depend strongly on the location of the particle on the bump. We now investigate the location dependence of these time-averaged aerodynamic forces.

This section presents the time-averaged results of the flow over a particle positioned on different locations of the hemisphere. The instantaneous LES results are averaged over time period of 5500 dimensionless time (tU/d) units.

We first investigate the mean pressure coefficient, C_p, and mean skin friction coefficient, C_f, for the test particle at the top of the bump ($\theta \sim 90^o$). Shown (Figure 20) is the angular dependence of these quantities going around the test particle; note the difference in angular dependence between the top and bottom surfaces of the test particle. These are compared with the experimental results of Kim and Durbin [34] and Seidl et al [35]. However, only a qualitative comparison should be made due to the different Reynolds number and geometry.

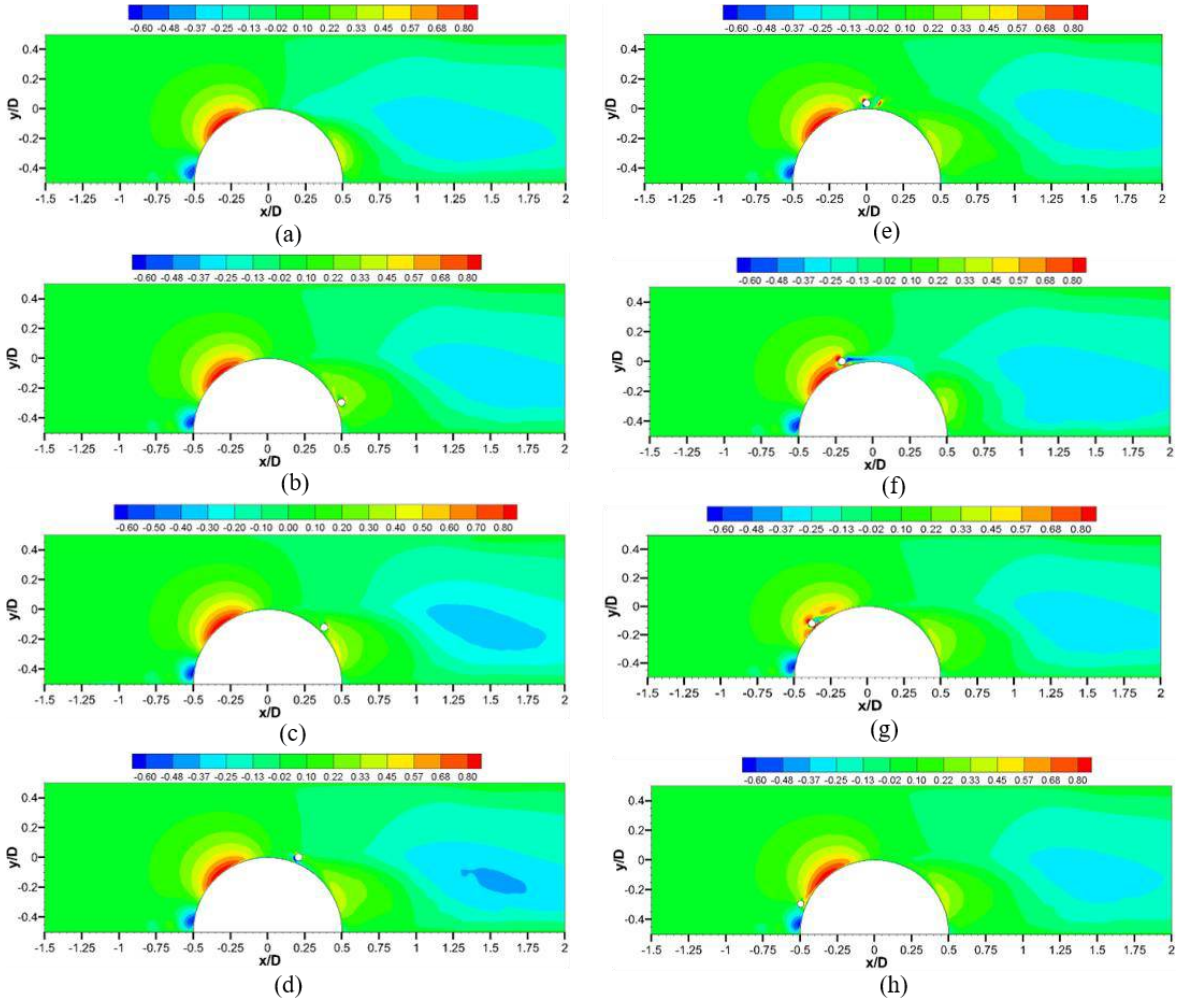

Fig. 15. Mean wall-normal velocity contours.

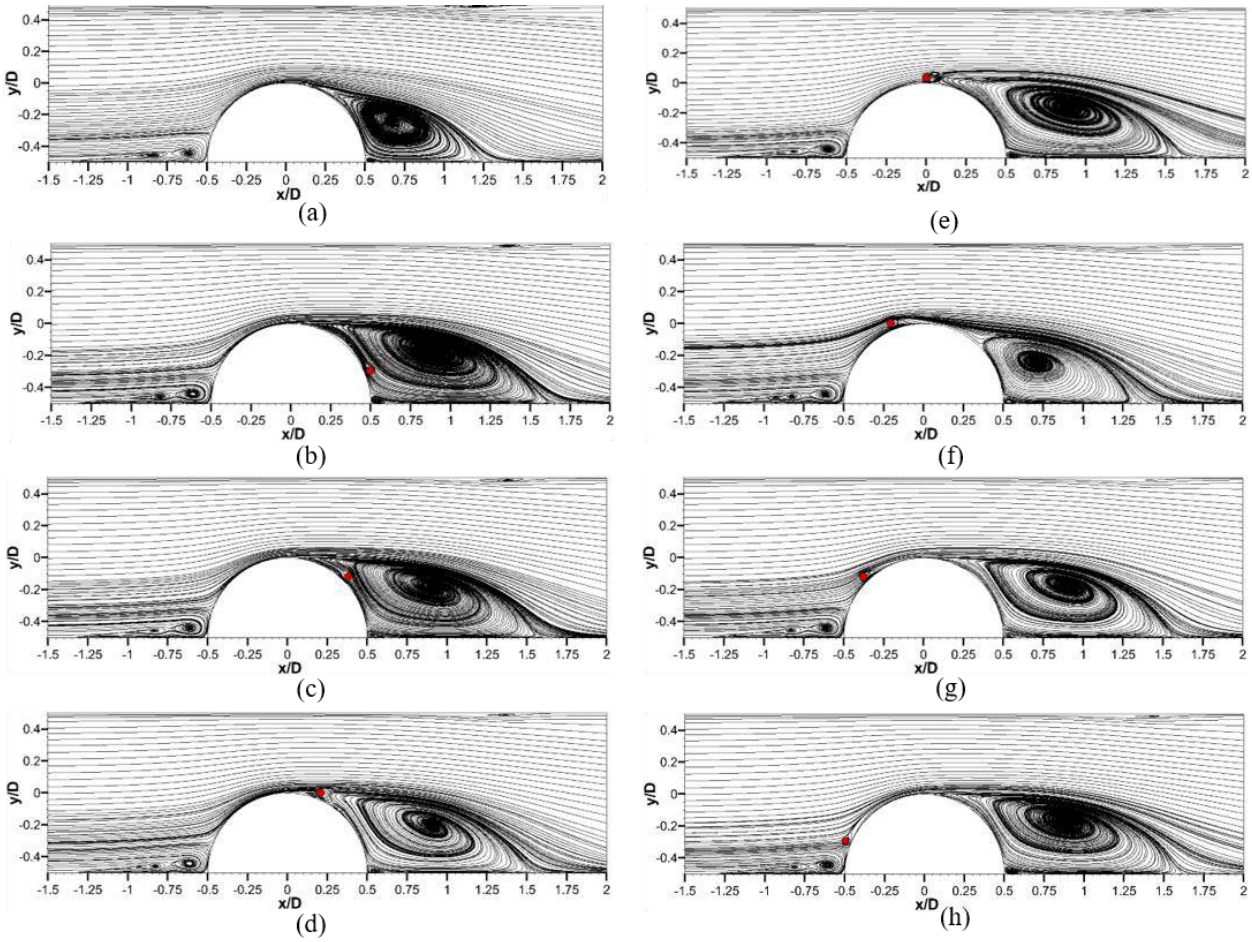

Fig. 16. Streamlines.

TABLE 1

Cases	Seperation angle (degrees)	Stagnation angle (degrees)	Reattachment length (x/D)
PB	89.74	159.44	1.31
PBP22.5	82.59	159.60	1.65
PBP45	82.89	159.69	1.64
PBP67.5	83.06	159.60	1.59
PBP90	84.82	159.35	1.68
PBP112.5	43.88	159.60	1.37
PBP135	80.61	159.60	1.63
PBP157.5	83.74	162.46	1.65

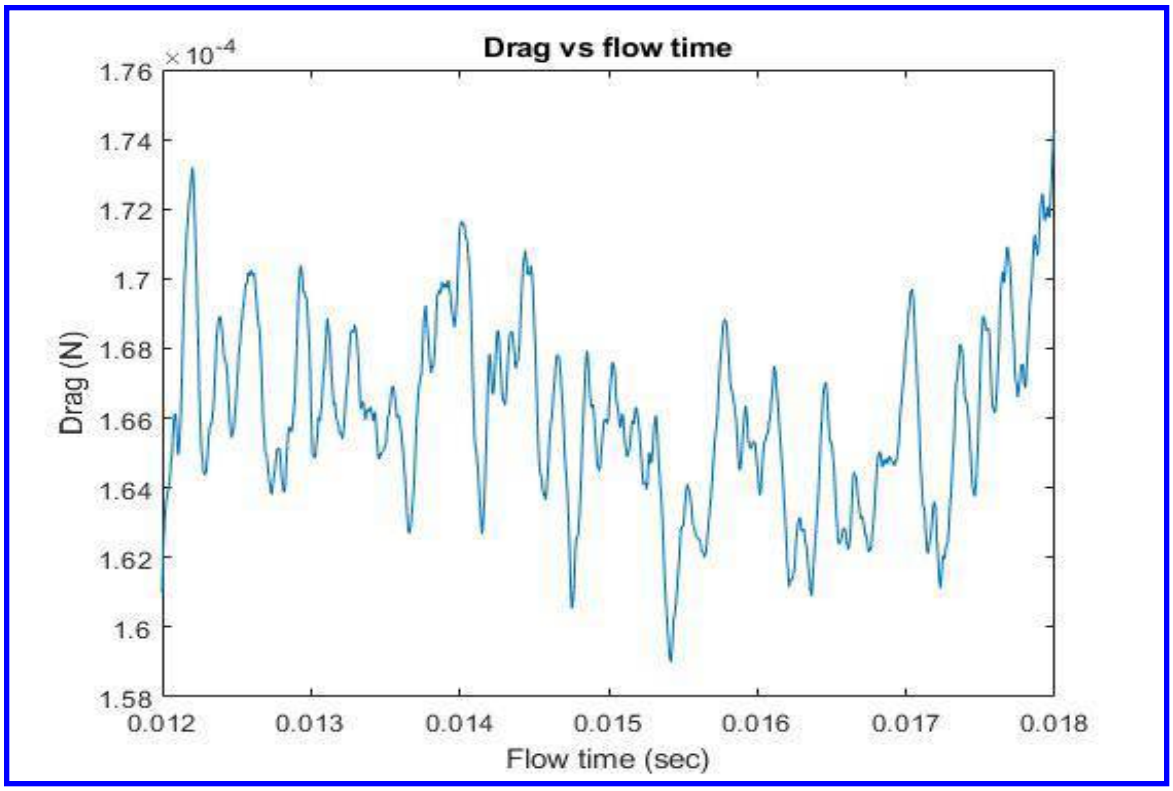

Fig. 17. Temporal history of drag on test particle at top of bump.

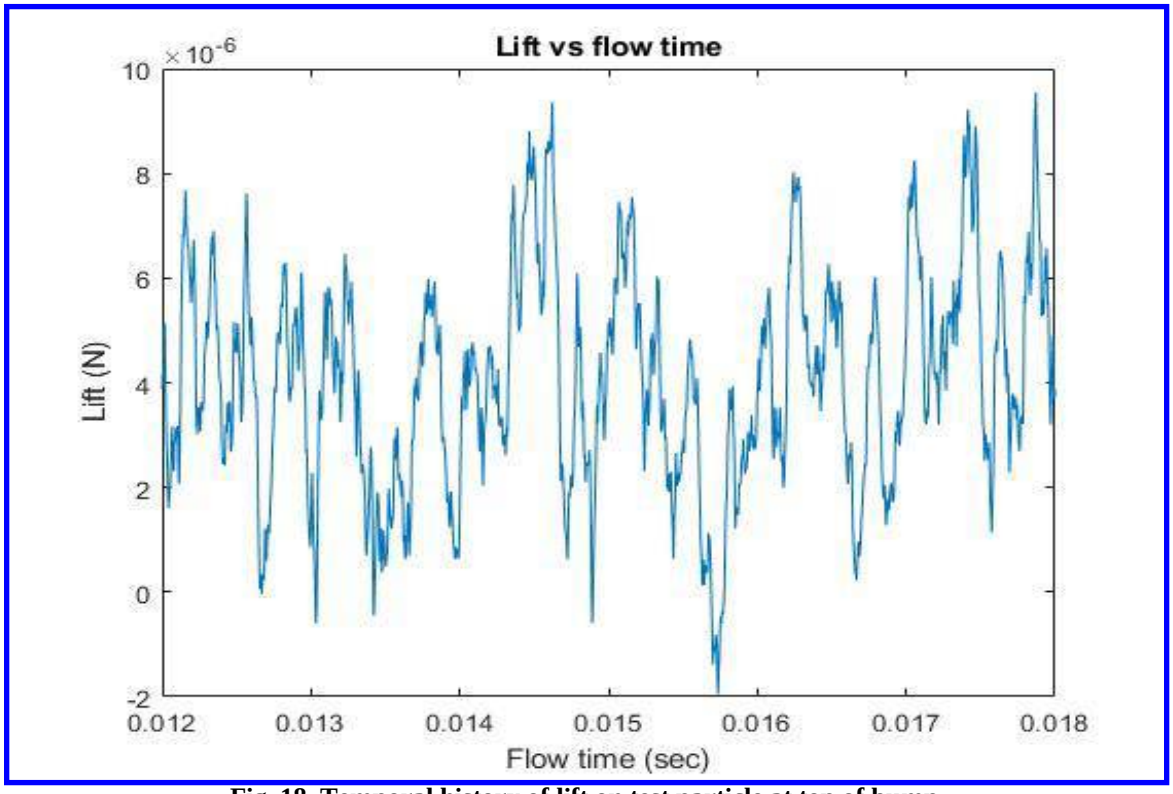

Fig. 18. Temporal history of lift on test particle at top of bump.

We now investigate the change in pressure coefficient and skin friction coefficient, as the test particle is moved to different locations on the bump. The angular position, α, of the particle is measured from right to left (Fig. 4 geometry). Since the flow over the test particle is not symmetric (above and below), C_p and C_f differ on the top and bottom of the set particle.

Fig. 21 a, b, and c show the angular dependence of C_p for the particle located on the downstream side of the bump i.e. in the recirculation zone. Initially, C_p is higher on the rear of the particle, but as the test particle is moved up the hill, Cp is higher on the front of the particle; this behavior results from the test particle being moved through the recirculation zone, with the flow changing direction in the vicinity of the bump and reversing how it hits the test particle in the different locations.

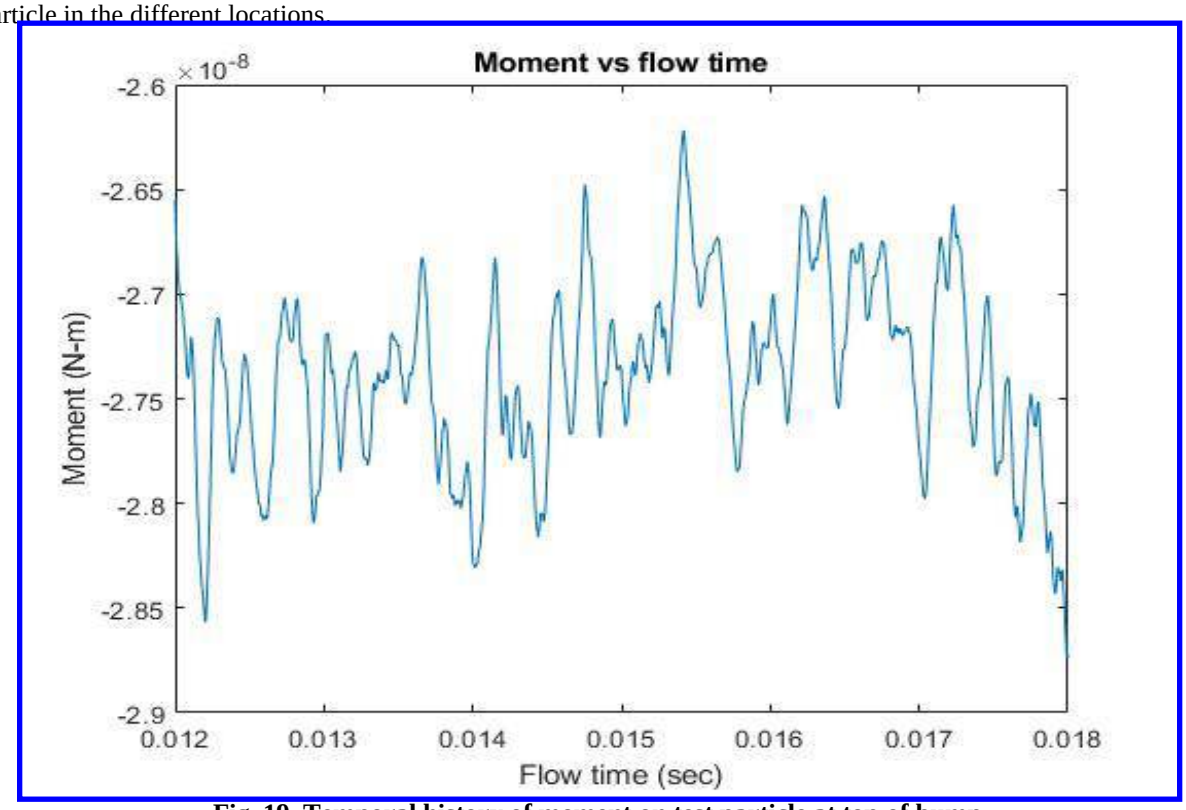

Fig. 19. Temporal history of moment on test particle at top of bump.

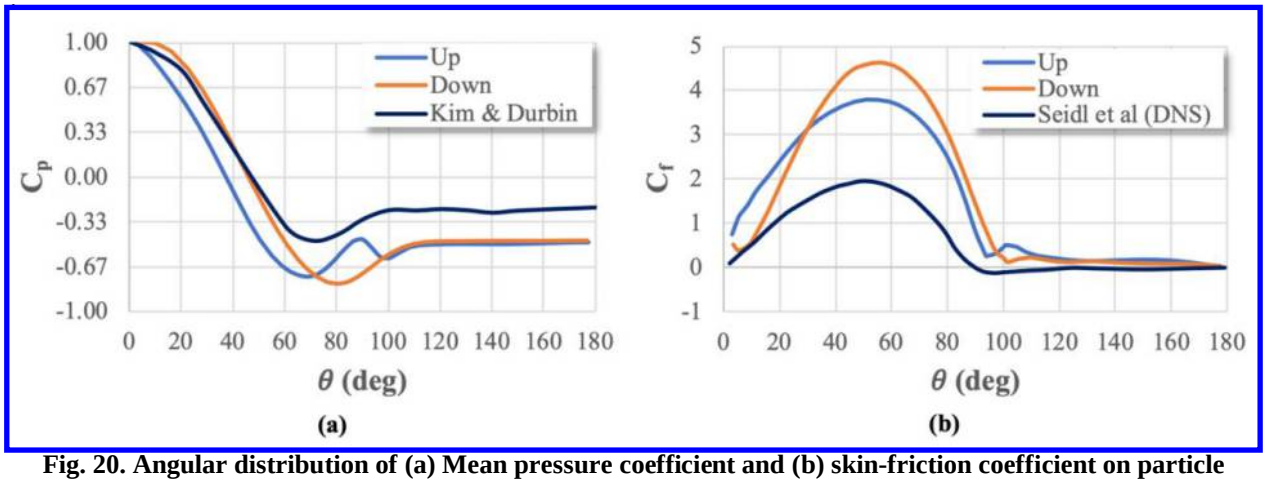

Fig. 20. Angular distribution of (a) Mean pressure coefficient and (b) skin-friction coefficient on particle located on the top of the hemispherical obstruction and compared with experimental and DNS results.

Fig. 21 d, e, and f show the angular distribution of C_p for the particle located on the upstream side of the bump. In fig. 21 d and e the flow directly hits the particle at the front, which results in high Cp in the front of the particle. In Fig 21 f, high C_p occurs behind the particle; this behavior is due to the particle being positioned just above the recirculation zone, which leads to high pressure near the particle and bump and hence to a high C_p.

Figure 22 a, b and c show C_f for the particle located on the downstream side of the bump. On the upper portion of the particle C_f is much smaller than on the bottom half of the particle. As the test particle moves up the bump, this difference disappears (fig. 20 b, where the particle is located at the top of the bump). This behavior is due to the particle moving through the recirculation zone, with the flow direction changing sign near to the bump. While moving up, it hits the bottom part of the particle which results in a high friction coefficient compared to the upper half. Fig. 22 d, e, and f show the angular distribution of C_f for the particle located on the upstream side of the bump.

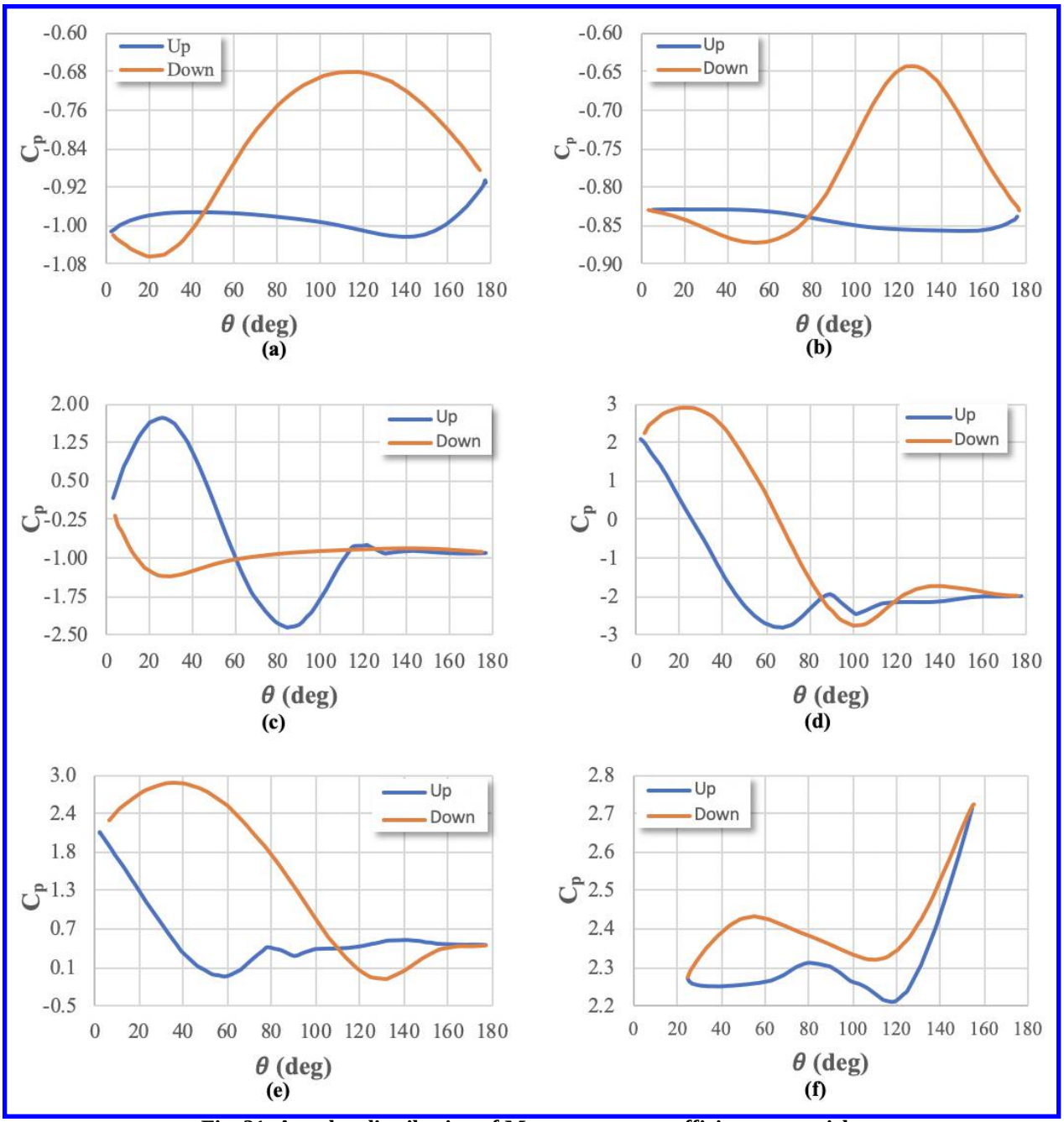

Fig. 21. Angular distribution of Mean pressure coefficient on particle.

Integrating the pressure and skin friction coefficients around the test particle surface allows for a calculation of the net aerodynamic forces on the test particle.

Mean drag, lift, and Moment:

Figure 23 shows the mean drag for the different angular locations of the particle on the bump. We have included error bars to indicate the standard deviation of the time-dependent drag. As the particle moves from the downstream to the upstream side of the bump, the mean drag increases (to a maximum of $F_{drag} \sim 0.29$ mN at $\alpha \sim 112.5_o$) and then decreases as the particle is moved to the upstream side of the bump. The standard deviation of the drag is higher on the downstream side of the bump. This behavior is due to the shear layer instability in the wake of the bump, which leads to the large temporal variation of the drag.

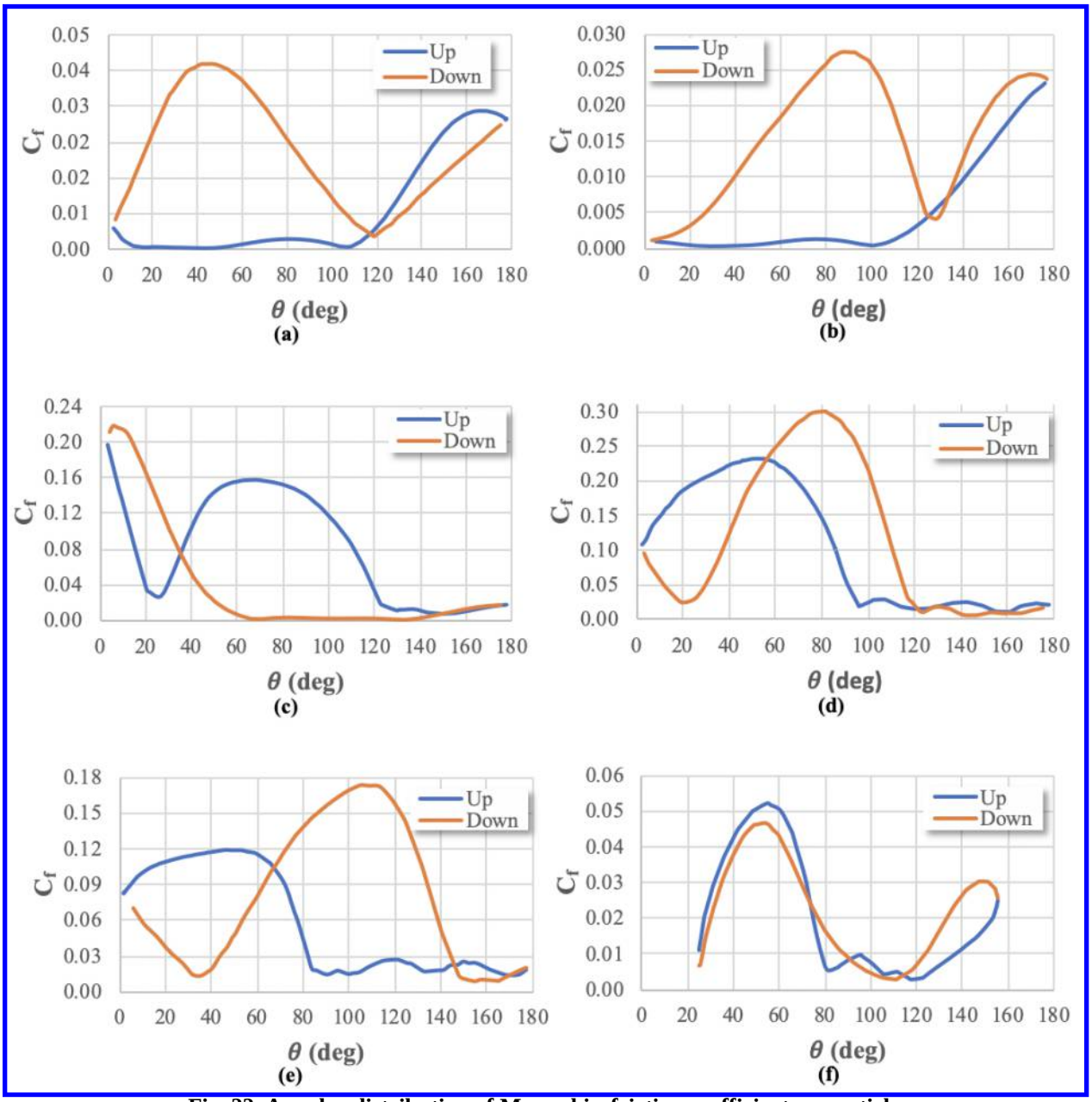

Fig. 22. Angular distribution of Mean skin-friction coefficient on particle.

Figure 24 presents the mean lift for the different angular locations of the particle on the bump. Again, the error bars indicate the standard deviation of the temporal variation of the lift. As the particle is moved from the downstream to the upstream side of the bump, the mean lift slightly decreases when the particle reaches the top of the bump and then strongly increases (to a maximum at $\alpha \sim 112.5^{o}$) and then decreases as the particle is moved to the upstream side of the bump. The temporal variation of the lift is high on the downstream side of the bump, again reflecting the influence of the vortex shedding.

Figure 25 shows the mean moment for the different angular locations of the particle on the bump. The moment is maximum for the test particle located at the top of the bump ($\theta \sim 90^{o}$). The temporal variation in the moment is everywhere small.

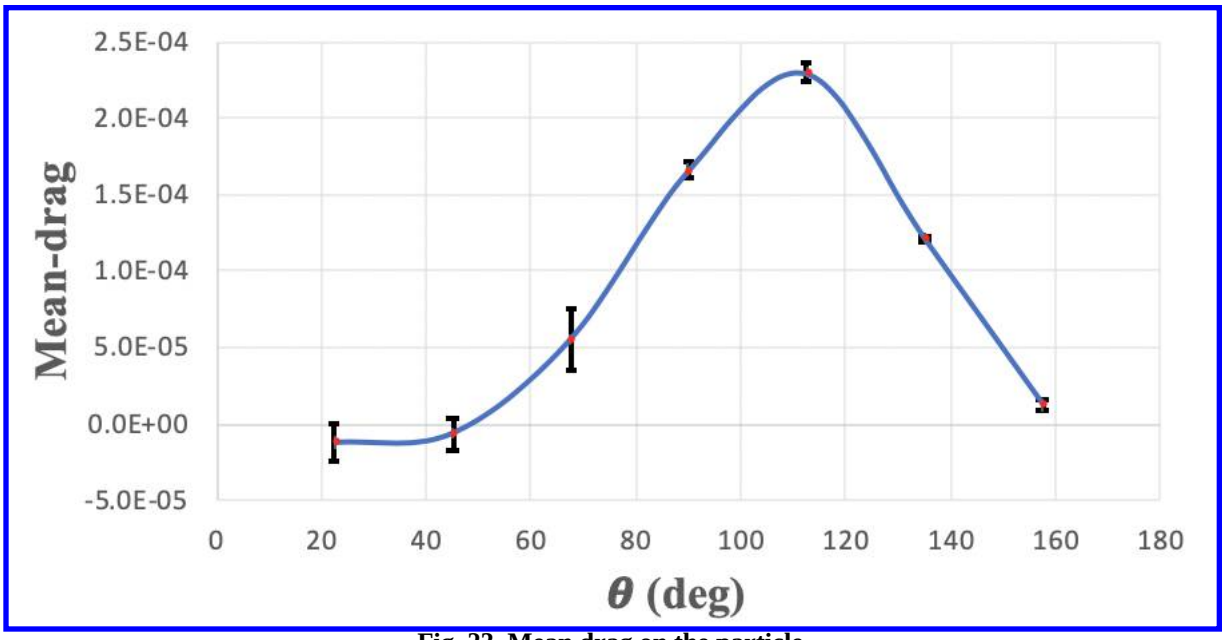

Fig. 23. Mean drag on the particle.

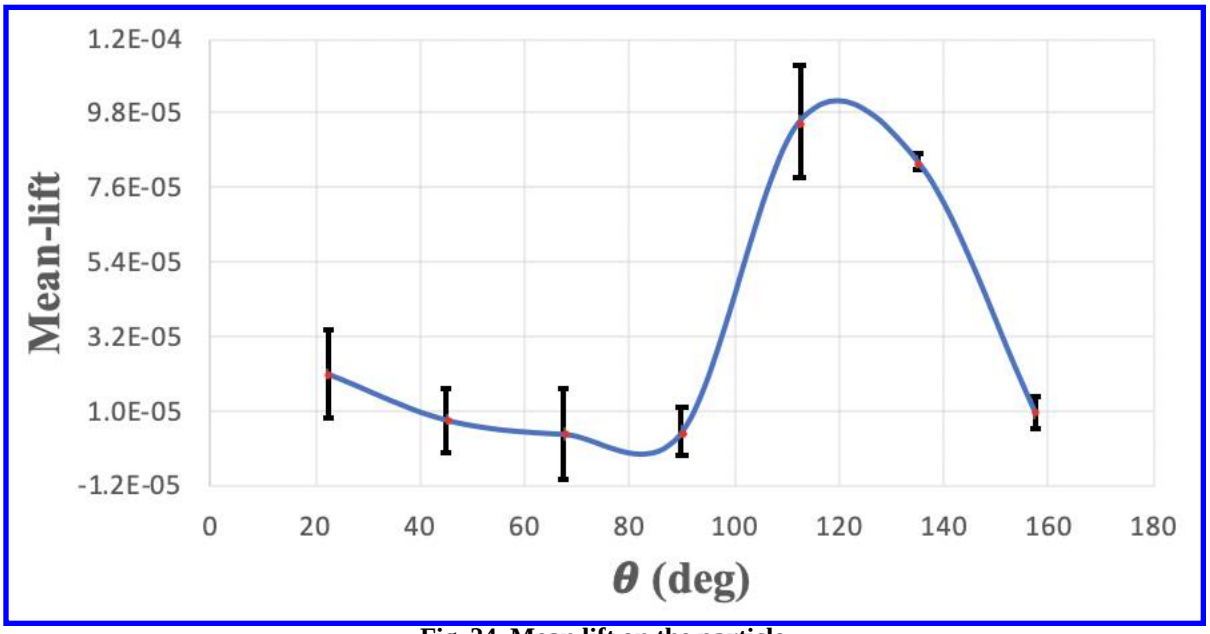

Fig. 24. Mean lift on the particle.

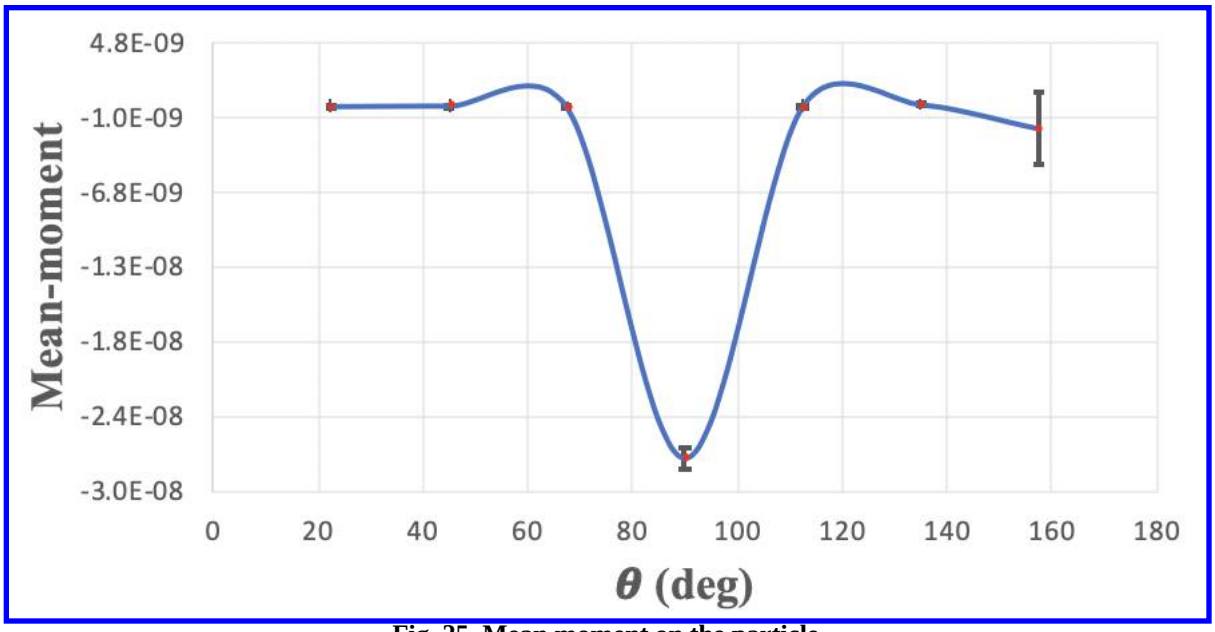

Fig. 25. Mean moment on the particle.

Conclusions

As a first step towards understanding the aerosolization of powder in a tube (as is appropriate for the injection phase of the Venturi Dustiness Tester), we have studied the aerodynamics of flow past an obstruction in a tube at Re ~ 20,000. The turbulent flow is characterized by two vortical processes: vortex necklace formation as the flow impinges on the obstruction, and vortex shedding from the top of the obstruction. Large Eddy Simulation has been used in order to capture the intricate vortex dynamics. Despite the complex dynamics, the time-averaged flow gives rise to a spatial variation in the drag, lift and moment of a test particle, as it is situated at various locations on the surface of the obstruction, reminiscent of a similar variation that occurs in the laminar regime (Re ~ 1000). This variation in the aerodynamic forces on surface particles will clearly be important in the aerodynamic disintegration of the powder hill.

Acknowledgments

This work is supported by the National Institute for Occupational Safety and Health (NIOSH). The authors gratefully thank the Ohio Supercomputer Center (OSC) and the Department of Mechanical and Materials Engineering, University of Cincinnati, for providing computational resources.

Disclaimer

The findings and conclusions in this paper are those of the authors and do not necessarily represent the views of the National Institute for Occupational Safety and Health. Mention of any product or company name does not constitute endorsement by the Centers for Disease Control and Prevention.

None of the authors has a financial relationship with a commercial entity that has an interest in the subject of this paper.

References

[1] Andreasen, A.H.M., Hoffman-Bang, H., and Rasmussen, N.H. (1939). On the ability of materials to be dusty. *Kolloid-Zeitschrift 86*: 70-77 [in German].

[2] Bakic, V., Experimental investigation of turbulent flows around a sphere. Ph.D. Thesis, TUHH Hamburg, Germany (2002).

[3] BOHS (1988). British Occupational Hygiene Society Technology Committee Working Party on Dustiness Estimation (Davies, K.M., Hammond, C.M., Higman, R.W. and Wells, A.B.) Progress in dustiness estimation. *Ann. Occ. Hyg. 32*: 535-544.
[4] Boundy, M., Leith, D. and Polton, T. (2006) Method to evaluate the dustiness of pharmaceutical powders. *Ann. Occ. Hyg. 50*: 453-458.
[5] Breum, N.O., Nielsen, B.H., Nielsen, E.M., Midtgaard, U. and Poulsen, O.M. (1997) Dustiness of compostable waste: a methodological approach to quantify the potential of waste to generate airborne micro-organisms and endotoxin. *Waste Management & Research 15*: 169-187.
[6] Breum, N.O. (1999) The rotating drum dustiness tester: variability in dustiness in relation to sample mass, testing time, and surface adhesion. *Ann. Occ. Hyg. 43*: 557-566.
[7] Brouwer, D. (2010) Exposure to manufactured nanoparticles in different workplaces. *Toxicology 269*: 120-127.
[8] Cawley, B. and Leith, D. (1993) Bench-top apparatus to examine factors that affect dust generation. *Appl. Occ. Env. Hyg. 8*: 624-631.
[9] Chung, K.Y.K. and Burdett, G.J. (1994) Dustiness testing and moving towards a biologically relevant dustiness index. *Ann. Occ. Hyg. 38*: 945-949.
[10] Cowherd, Jr., C., Grelinger, M.A. and Wong, K.F. (1989) Dust inhalation exposures from the handling of small volumes of powders. *Am. Ind. Hyg. Assoc. J. 50*: 131-138.
[11] Dubey, P., Ghia, U. and Turkevich, L.A. (2017). Computational fluid dynamics analysis of the Venturi Dustiness Tester. *Powder Technology 312*: 310-320.
[12] Dhamankar, N. S., Blaisdell, G. A., & Lyrintzis, A. S. (2017). Overview of turbulent inflow boundary conditions for large-eddy simulations. *Aiaa Journal*, *56*(4), 1317-1334.
[13] Evans, D. E., Turkevich, L.A., Roettgers, C.T., Deye, G.J. and Baron, P.A. (2013) Dustiness of fine and nanoscale powders. *Ann. Occ. Hyg. 57*: 261-277.
[14] Hamelmann, F. and Schmidt, E. (2003) Methods for characterizing the dustiness estimation of powders—a review. *KONA 21*: 7–18.
[15] Hamelmann, F. and Schmidt, E. (2004) Methods for characterizing the dustiness estimation of powders. *Chem. Eng. Technol. 27*: 844–847.
[16] Hammond, C.M. (1980) Dust control concepts in chemical handling and weighing. *Ann. Occ. Hyg. 2*: 95-109.
[17] Heitbrink, W.A., Baron, P.A. and Willeke, K. (1992) An Investigation of dust generation by free falling powders. *Am. Ind. Hyg. Assoc. J. 53*: 617-624.
[18] Hjemsted, K. and Schneider, T. (1996a) Dustiness from powder materials. *J. Aerosol Sci. 27:* S485-S486.
[19] Lidén, G. (2006) Dustiness testing of materials handled at workplaces. *Ann. Occ. Hyg. 50:* 437–439.
[20] Mathey, Fabrice, et al. "Assessment of the vortex method for large eddy simulation inlet conditions." *Progress in Computational Fluid Dynamics, An International Journal* 6.1-3 (2006): 58-67.
[21] Ogura, I., Sakurai, H. and Gamo, M. (2009) Dustiness testing of engineered nanomaterials. *J. Physics: Conference Series 170*: 012003, 1-4. [*Nanosafe 2008*: *International conference on safe production and use of nanomaterials*]
[22] Palakurthi, N.K. (2016) Numerical investigation of particle aerodynamics in a laminar boundary layer flow. M.S. thesis, University of Cincinnati.
[23] Palakurthi, N.K., Ghia, U. and Turkevich, L.A. (2019). Aerodynamics of a particle on a hill: numerical investigation of powder aerosloization in the Venturi dustiness tester (in review).
[24] Plinke, M.A.E., Leith, D., Holstein, D.B. and Boundy, M.G. (1991) Experimental examination of factors that affect dust generation. *Am. Ind. Hyg. Assoc. J. 52*: 521-528.
[25] Plinke, M.A.E., Maus, R. and Leith, D. (1992) Experimental examination of factors that affect dust generation by using Heubach and MRI testers. *Am. Ind. Hyg. Assoc. J. 53*: 325–330.
[26] Plinke, M.A.E., Leith, D., Boundy, M.G. and Löffler, F. (1995) Dust generation from handling powders in industry. *Am. Ind. Hyg. Assoc. J. 56***:** 251–257.
[27] Pope, S. B. (2001*). Turbulent flows* (Cambridge: Cambridge University Press)
[28] Schulte, P., Geraci, C., Zumwalde, R., Hoover, M. and Kuempel, E. (2008). Occupational risk management of engineered nanoparticles. *J. Occ. Env. Hyg. 5:* 239-249.
[29] Sakamoto, Haniu, and H. Haniu. "A study on vortex shedding from spheres in a uniform flow." (1990): 386-392.
[30] Savory, E., and N. Toy. "Hemisphere and hemisphere-cylinders in turbulent boundary layers." *Journal of Wind Engineering and Industrial Aerodynamics* 23 (1986): 345-364.
[31] Tomboulides, A., S. Orszag, and G. Karniadakis. "Direct and large-eddy simulations of axisymmetric wakes." *31st Aerospace Sciences Meeting*. 1993.
[32] Wood, J. N., De Nayer, G., Schmidt, S. and Breuer, M. (2016) Experimental investigation and large-eddy simulation of the turbulent flow past a smooth and rigid hemisphere. *Flow, Turbulence and Combustion 97*: 79-119.
[33] Celik, I. B., Cehreli, Z. N., & Yavuz, I. Index of resolution quality for large eddy simulations (2005).
[34] Kim, H. J., & Durbin, P. A. (1988). Observations of the frequencies in a sphere wake and of drag increase by acoustic excitation. The Physics of fluids, 31(11), 3260-3265.
[35] Seidl, V., Muzaferija, S., & Perić, M. (1997). Parallel DNS with local grid refinement. Applied Scientific Research, 59(4), 379-394.